AIMS Materials Science, 10(4): 637–651.
DOI: 10.3934/matersci.2023036
Received: 14 May 2023
Revised: 24 July 2023
Accepted: 26 July 2023
Published: 09 August 2023

http://www.aimspress.com/journal/Materials

Research article

Conflicting behavior between powdering and flaking resistance under skin pass mill process in galvannealed interstitial free steel

Hyungkwon Park[1,*], Young-Joong Jeong[2], Jin-Jong Lee[1], Chang-Hoon Lee[1], Bong Joo Goo[2] and Yonghee Kim[2]

[1] Department of Steels, Advanced Metals Division, Korea Institute of Materials Science, 797 Changwondae-ro, Seongsan-gu, Changwon, Gyeongnam 51508, Republic of Korea
[2] Research & Development (R&D) center, Hyundai Steel Company, 1480, Bukbusaneop-ro, Songak-Eup, Dangjin-Si, Chungnam 31719, Republic of Korea

* **Correspondence:** E-mail: hpark@kims.re.kr; Tel: +82-55-280-3444; Fax: +82-55-280-3599.

Abstract: The failure of galvannealed (GA) coatings during press forming is an important issue for steel companies, because it results in a deteriorated product quality and reduced productivity. Powdering and flaking are thought to be the main failure modes in GA steel. However, these two modes currently lack a clear distinction, despite their different failure types. Therefore, in this study, we demonstrate that the different behaviors of these two failure modes are generated by the skin pass mill (SPM) condition and we discuss the underlying mechanism in detail using microstructural and simulation analyses. With the increase in steel elongation from 0% to 4.0% under milling force from 0 to 6 ton, a high compressive stress is produced up to −380 MPa on the surface of the steel sheet and the interface is correspondingly flattened from 0.96 to 0.53 μm in Ra. This flattening weakens the mechanical interlocking effect for adhesive bonding, deteriorating the flaking resistance from 41.1 to 65.2 hat-bead contrast index (hci). In addition, the GA coating layer becomes uniformly densified via the filling of pores under compressive stress in the layer. Furthermore, the ζ phase exhibits significant plastic deformation, leading to a uniform coverage of the coating surface; this helps to suppress crack propagation. Accordingly, the powdering resistance gradually improves from 4.2 to 3.5 mm. Consequently, with the increase in SPM-realized steel sheet elongation, the powdering resistance improves whilst the flaking resistance deteriorates. Significantly for the literature, this implies that the two failure modes occur via different mechanisms and it indicates the possibility of controlling the two coating failure modes via the SPM conditions.

Keywords: galvannealed steel; coating failure; skin pass mill; interstitial free steel; finite element modeling

1. Introduction

Galvannealed (GA) steel is an Fe-Zn-coated steel produced by post-annealing immediately after pure Zn coating [1–3]. During annealing, Fe (in the steel substrate) and Zn (in the coating layer) are inter-diffused by the thermal driving force, leading to the formation of an Fe-Zn intermetallic compound (IMC). Accordingly, the GA coating consists of several Fe-Zn IMCs including Γ (Fe_3Zn_{10}), Γ_1 (Fe_5Zn_{21}), δ ($FeZn_{10}$) and ζ ($FeZn_{13}$) phases [1–4]. Because GA steel exhibits good weldability, paintability and corrosion resistance, it is widely used in the automotive industry [1,2,5–7].

Fe-Zn IMCs are relatively hard and brittle compared to pure Zn ones. Therefore, the coating can be damaged and undergo failure during press forming [2,3]. Fragments accumulate on the press die, which can lead to surface defects. In addition, the coating is locally delaminated and the bare substrate occasionally exposed. This reduces the product quality. Hence, failure of the coating layer represents an issue for steel companies and many researchers have studied the mechanism of coating failure, in the hope of developing evaluation and prevention methods [8–10].

Two types of failure have been reported: powdering and flaking [1,2,8,11]. Powdering refers to a fine particle-type fragment that becomes detached from the coating interior [2,12]. Hence, its main cause is the brittleness of the coating layer, particularly the δ phase [13]. Conversely, flaking is a failure that occurs at the interface between the coating layer and substrate. Here, the fragment is a thin flake. It is an interfacial failure and the Γ phase is located at the bottom of the GA coating. Hence, flaking is thought to be predominantly caused by bond failure between the Γ phase and substrate. Meanwhile, when the Fe content in the coating layer increases (Fe-Zn alloying proceeds by varying the annealing time and/or temperature), the fraction of the relatively brittle phase increases [2]. The increased fraction of Fe in the δ phase produces a more brittle phase, which aggravates the powdering resistance [14]. In addition, the Γ phase also becomes consistently thicker under increasing Fe content in the coating layer. From this point, it is commonly understood that the thickness of the Γ phase relates to the flaking resistance [13,15]. Consequently, it appears that the two coating failures tend to simultaneously deteriorate under increasing Fe content and the two failure modes have occasionally been confoundable.

Cheng et al. suggested that many researchers tend to consider the two failure modes as interchangeable because of the nature of laboratory test methods and the difficulty in separating the two modes [13]. In addition, the coinstantaneous occurrence of the two failure modes and their similar tendencies with respect to the increase in Fe content impedes clear discrimination. However, the behaviors of the two failure modes are not identical. Strictly speaking, they proceed via different mechanisms. For example, flaking relates to the interfacial adhesive bonding between the Γ phase and substrate, whereas powdering is relevant to cohesive bonding in the coating layer. Park et al. demonstrated that powdering and flaking failures do not always occur with the same tendencies [16]. Consequently, the two failure modes should be clearly distinguished and viewed from different perspectives to improve the two different resistances.

Skin pass milling (SPM) is a process generally applied to cold-rolled and GA steels to improve surface quality and thickness uniformity and reduce the yield point phenomenon. After SPM, the GA

coating surface becomes locally flattened and the surface roughness changes slightly depending on the SPM conditions. It has been reported that the surface roughness relates to the adhesive bonding strength associated with flaking resistance [17]. Park et al. reported that the average roughness of a GA coating surface is significantly affected by its crater density [16]. Furthermore, crater formation increases the interfacial roughness, which determines the adhesive bonding strength. Moreover, Hamers et al. have demonstrated that SPM simultaneously reduces the surface and interfacial roughness [17]. Therefore, it can be inferred that the SPM process influences the adhesive strength of the GA coating as well as the flaking resistance.

In this study, a GA sheet was rolled using an SPM simulator to investigate the effect of SPM on powdering and flaking behaviors. Two typical evaluation methods, V-bending and hat-channel drawing with a bead (referred to as a hat-bead test) were applied to evaluate the powdering and flaking resistances, respectively. Notably, the different behavior between powdering and flaking was found as a percentage reduction in the thickness of the increased sheet (i.e., increased rolling force). That is, interestingly, the powdering resistance increased, whereas the flaking resistance decreased. It directly demonstrates that the two failures are generated by different mechanisms and the reason of the different behavior is explained based on the experimental and numerical results. It is crucial to understand the mechanisms of two failure modes to reduce defective products and improve the product quality. In addition, from this result, the possibility to control the level of powdering and flaking via SPM is suggested.

2. Materials and methods

2.1. Experimental details

In this study, a Ti-stabilized interstitial-free (IF) steel sheet with a thickness of 0.712 mm was used; its chemical composition is listed in Table 1. The sheet was GA-coated via a continuous galvanizing line (CGL), recrystallized at 840 ℃, coated in a zinc bath at 460 ± 1 ℃ and underwent galvannealing at 500 ℃. The Al content in the bath was controlled at 0.128 ± 0.009 wt% and the line speed was set to 140 mpm. The average coating weight of the GA coating layer was 46.6 g/m^2 and the Fe content was 11.3 wt%. The as-coated sample was obtained without SPM to investigate the effect of SPM on the powdering and flaking behaviors.

In this experiment, the as-coated sample was skin-passed using an SPM simulator. The sample was cut to 70 × 500 mm^2 and cleaned using ethanol prior to SPM. Then, the sheet was put between top and bottom rolls and elongated, and the degree of elongation was controlled by millingforce. 0, 3, 3.25, 4, 5 and 6 tons and the sheet was correspondingly elongated to 0%, 0.8%, 1.0%, 1.8%, 2.7% and 4.0% and thinned to 0.712, 0.706, 0.705, 0.699, 0.693 and 0.684 mm, respectively. For convenience, the as-coated and 0.8%, 1.0%, 1.8%, 2.7% and 4.0% elongated samples are denoted as No-SPM, 0.8-SPM, 1.0-SPM, 1.8-SPM, 2.7-SPM and 4.0-SPM, respectively.

Table 1. Chemical composition of GA IF steel.

Chemical composition (wt%)								
C	Si	Mn	P	S	Al	N	Ti	Nb
0.0012	0.002	0.065	0.0099	0.0054	0.032	0.0021	0.032	0.009

To evaluate the mechanical properties of the coating layer, V-bending and hat-bead tests were

performed and the resistances to powdering and flaking were evaluated [8,16]. Specimens with dimensions of 110 × 70 mm^2 and 50 × 245 mm^2 were prepared for V-bending and hat-bead tests, respectively. Each sample was cleaned with ethanol before experiments. In the V-bending test, the specimen was V-shaped with a 60° tip and flattened using a flat die. Adhesive tape was applied to the V-bent region, and the gaps between the fragments on the tape were evaluated. In the hat-bead test (Chongro Scientific Co., Ltd.), the clamping force, punching speed and drawing height were set to 30, 300 and 65 mm, respectively. In addition, a bead of radius 3 mm was applied. Subsequently, the bottoms of the formed specimens' vertical walls were taped and the contrast of the tape was evaluated using the hat-bead contrast index (hci). Each method has been described in the literature [8,10,18].

The chemical composition of the steel sheet was measured using inductively coupled plasma atomic emission spectrometry (ICP-AES, ARCOS EOP, Spectro). To observe the morphology of the coating surface and interface, a scanning electron microscope (SEM, Phenom XL, Thermo Fisher Scientific) in the backscattered electron mode was applied (alongside the 3D morphology in the case of the interfacial microstructure). For interface observation, the coating layer was selectively removed without substrate dissolution, using a solution mixture of 500 mL HCL with 3.5 g hexamethylene tetraamine and 500 mL deionized water. Hexamethylene tetraamine was used as an inhibitor to protect the Fe substrate from etching. The cross-section of the coating layer was observed using field-emission scanning electron microscopy (FE-SEM, JSM-7001F, JEOL) in the secondary electron mode. The samples were mounted, polished and then ion-etched to distinguish each Fe-Zn IMC phase. Furthermore, the phase fractions of each coating, η, ζ, δ and Γ (Γ + Γ_1), were characterized by X-ray diffraction (XRD, D8 ENDEAVOR, Bruker). The XRD patterns were quantitatively analyzed using the Rietveld method [15,19]. The topographies of the coating surface and interface were measured using a surface profilometer (Surfcom 1500SD2, ACCRETACH).

2.2. Finite element analysis

To analyze the deformation behavior of the steel sheets during SPM, the finite element method (FEM) was applied using the commercial rigid-plastic finite element code DEFORM-2D. To reduce the computational time, a relatively simple model was designed involving a four-node element mesh, as shown in Figure 1. In the modeling, the top and bottom rolls were assumed to be rigid bodies and mesh analysis was applied to the steel sheet. After preliminary simulation trials to optimize the numerical model in terms of a mesh sensitivity analysis, the numbers of initial meshes and nodes were set to 7124 and 7686, respectively. The radius of the two rolls was set to 20 mm and the thickness of the steel sheet was 0.7 mm, as shown in Figure 1b.

The steel deformation was calculated using a well-known flow stress model, in which the yield stress under uniaxial conditions (as a function of strain, strain rate and temperature) can be considered as flow stress, via Eq 1 [20]:

$$\bar{\sigma} = \bar{\sigma}(\bar{\varepsilon}, \dot{\bar{\varepsilon}}, T) \tag{1}$$

where $\bar{\sigma}$, $\bar{\varepsilon}$, and $\dot{\bar{\varepsilon}}$ denote the flow stress, effective plastic strain and effective strain rate, respectively. When the applied stress exceeded the yield stress, the steel began to deform plastically. In addition, T was neglected because the experiment was performed at room temperature and the effect of temperature on the mechanical properties was negligible at 300 °C [21]. Moreover, the normalized Cockcroft & Latham damage criterion was used and the damage factor D_f was expressed as Eq 2 [20]:

$$D_f = \int_0^{\varepsilon_f} \frac{\sigma^*}{\sigma} d\varepsilon \quad (2)$$

where σ^* and σ denote the tensile maximum principal stress and effective stress, respectively. ε_f and $d\varepsilon$ denote the strain at the moment of fracture initiation and the effective strain increment, respectively. The damage factor can be used to predict the material fracture with respect to the damage intensity during cold forming and the value was set to 1.0 [18,22]. The material parameters of IF steel were obtained from our previous modeling [18]. The x- and y-axis stresses were measured at the monitoring gauge in the surface region, as shown in Figure 1b. In addition, the friction factor between the rolls and sheets was set to 1.2, which is specified in the DEFORM-2D library as a standard value for the cold forming of steel dies.

In the simulation, the top and bottom rolls were rotated at 10 RPM (angular velocity: 1.0472 rad/s) in opposite directions. The top roll turned counterclockwise whilst the bottom roll turned clockwise. The steel sheet intermediated between the two rolled at a velocity of 10 mm/s in the positive x direction. The velocity was determined by considering the linear velocities of the rolls. The degree of sheet elongation was simulated by controlling the gap between the two rolls. After the mesh elongation was measured in preliminary trials, the gap was controlled from 0.700 to 0.668 mm, corresponding to the labels No-SPM to 4.0-SPM. Additionally, in the 3D post analysis, the width of the top roll was set to 5 mm, whilst that of the bottom roll and steel sheet was set to 10 mm to analyze the distribution of the effective and y-axis stresses.

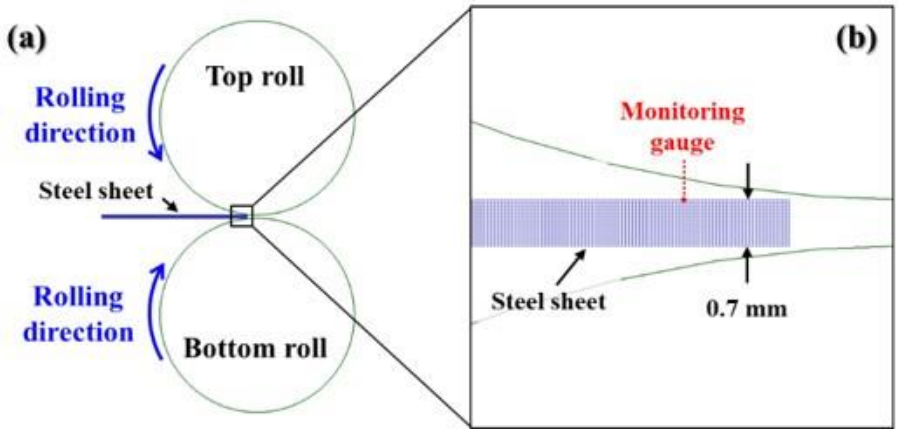

Figure 1. (a) Numerical modeling design and (b) detailed steel sheet mesh design.

3. Results and discussion

Figure 2 shows the changes in the powdering and flaking resistances under SPM elongation. In this study, SPM elongation refers to the SPM-realized elongation percentage of the sheet. In Figure 2a, the y axis (mm) denotes the width distribution of the fragments attached to the tape. When more fragments were detached from the GA sheet, the width increased, implying a reduction in the powdering resistance. Conversely, in Figure 2b, the unit of the y axis (hci) shows the contrast of the tape on which the fragments were stuck. A low hci (high contrast) indicates that small numbers of fragments were produced, implying high flaking resistance. Meanwhile, a high hci (low contrast) indicates large numbers of fragments, implying a low flaking resistance. It is worth noting that when

the SPM elongation increased, the powdering resistance increased (Figure 2a), whereas that of flaking decreased (Figure 2b). From this, it can be inferred that the two failure modes, powdering and flaking, arose via different mechanisms. That is, a high rolling force improved the powdering resistance but reduced the flaking resistance.

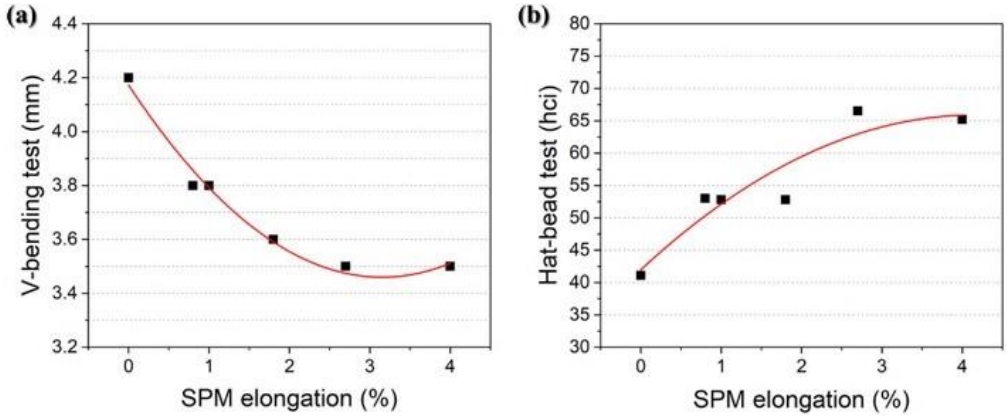

Figure 2. Graphs of the relations between (a) V-bending and SPM elongation and (b) hat-bead testing and SPM elongation.

From the samples, the No-, 1.8-, and 4.0-SPM specimens were selected, and their microstructures were analyzed in detail. Figure 3a–c shows the surface morphology of the No-, 1.8-, and 4.0-SPM specimens, respectively. When SPM elongation increased, the squashed area (rolling trail) widened. As shown in Figure 3a, the GA steel was entirely covered by the ζ phase on the top of the surface. In addition, it is noteworthy that several pothole regions marked by the yellow inverted triangles were found, which indicate craters. Craters are Zn-depleted regions where Zn is sucked into the adjacent outburst regions during galvannealing. They occur because Fe diffusion is comparatively more active at grain boundaries than grain interiors and a rapid growth of Fe-Zn alloying occurs at the grain boundary during outburst. Moreover, crater evolution affects the surface roughness [15,17]. Figure 3d–f shows the changes in the surface topography of the No-, 1.8- and 4.0-SPM specimens, respectively. The surface of the GA coating was markedly flattened. Figure 4a–c shows the change in average roughness (Ra), maximum height of the roughness profile (Rz) and peaks per inch (PPI) under the increase in SPM elongation. It can be confirmed that the surface is gradually flattened under the decrease in average roughness (Ra) from 1.20 to 0.47 μm (Figure 4a). In addition, the maximum height of the roughness profile (Rz) decreased from 9.13 to 5.42 μm (Figure 4b) and the number of peaks (i.e., the PPI) was reduced from 210 to 46 (Figure 4c). Consequently, it is reasonable to suggest that the coating surface becomes more flattened when the SPM elongation increases.

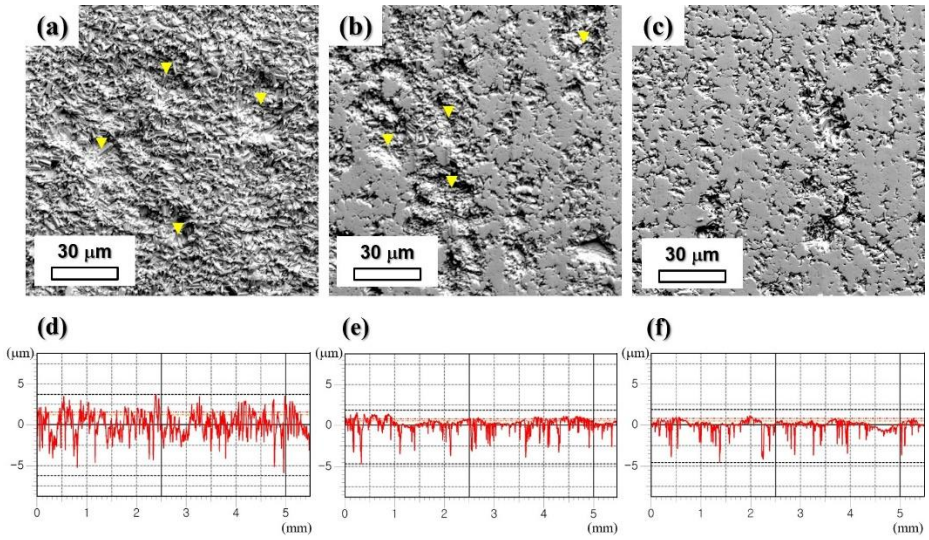

Figure 3. FE-SEM micrographs of coating surface morphology: (a) No-, (b) 1.8-, and (c) 4.0-SPM. Coating surface roughness of (d) No-, (e) 1.8- and (f) 4.0-SPM.

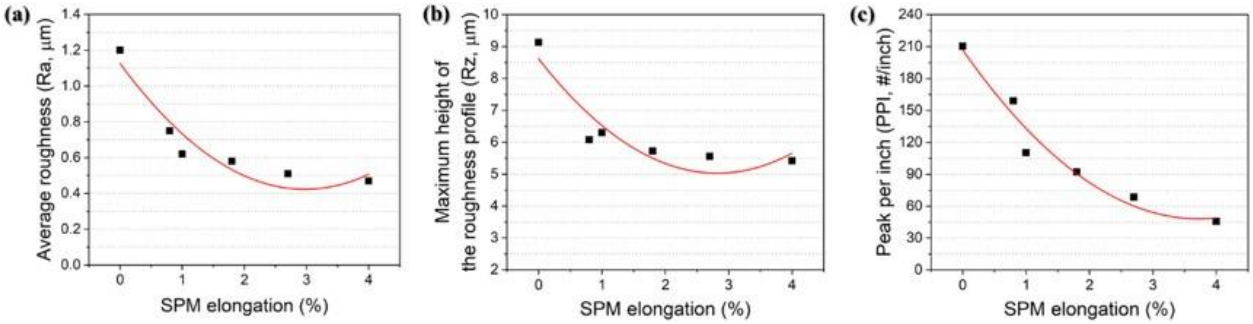

Figure 4. Coating surface profiles of each sample: (a) average roughness (Ra), (b) maximum height of the roughness profile (Rz) and (c) PPI.

Figure 5a–c shows the changes in the interfacial morphology and roughness of the No-, 1.8-, and 4.0-SPM specimens under SPM elongation, respectively. In each figure, the blue inverted triangles indicate the knoll region, whereas the open inverted triangles indicate the trace of the knoll. The knoll microstructure only evolved under the crater [16]. In addition, the height of the region remained slightly higher than that of the surrounding region and the top of the knoll exhibited an etch-pit morphology [15,16]. Therefore, the microstructure is related to the adhesive strength caused by the mechanical interlocking effect [16]. The knoll region was frequently observed in the No-SPM specimen in Figure 5a. However, it became difficult to identify the region with an increase in SPM elongation, as shown in Figure 5b,c. It appears that the knoll regions were mechanically compressed. Mechanical interface flattening is clearly shown in the 3D morphology (Figure 5d–f). Here, the color indicates the relative altitude difference. That is, the red and blue colors denote relatively high and relatively low regions, respectively. Clearly, the height difference gradually decreased under SPM elongation, indicating interface flattening. Finally, it is difficult to distinguish the rough knoll region (Figure 5f). Figure 5g–i show the interfacial roughness profiles under SPM elongation. It can be clearly confirmed that the interface morphology is flattened.

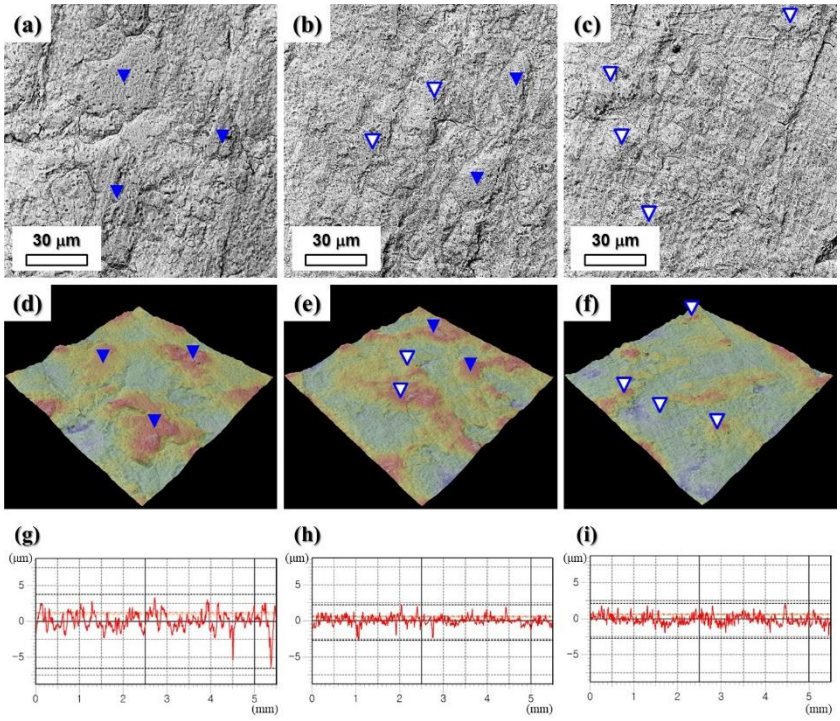

Figure 5. FE-SEM micrographs of the interfacial micro- structures of (a) No-, (b) 1.8- and (c) 4.0-SPM; (d–f) 3D morphology of (a–c) regions (the color in the 3D morphology indicates the relative altitude difference) and interface roughness of (g) No-, (h) 1.8- and (i) 4.0-SPM.

Figure 6a–c shows the changes in Ra, Rz and PPI of the interface under the increase in SPM elongation, respectively. The interface became even under the change in Ra from 0.96 to 0.53 μm with SPM elongation (Figure 6a). In addition, the maximum height of the interface decreased from 6.71 to 4.13 μm (Figure 6b) and the number of peaks was also reduced from 112.26 to 77.21 (Figure 6c). The roughness rapidly decreased up to ~2% elongation and subsequently remained approximately constant. As a result, the interface roughness correspondingly decreased with surface roughness as the SPM elongation increased. That is, the GA coating surface and the interface between the coating layer and substrate were simultaneously flattened.

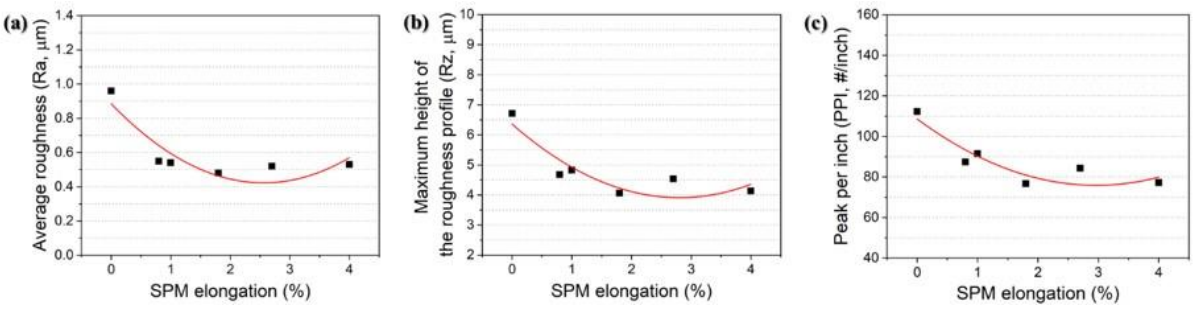

Figure 6. Interface profiles of each sample: (a) average roughness (Ra), (b) maximum height of the roughness profile (Rz) and (c) PPI.

Park et al. has reported that the bonding of a GA coating is reinforced by a mechanical interlocking effect [16]. In addition, the interface morphology evolves during crater formation. That is, a rough knoll region evolves just under the crater, as mentioned above [16]. Here, the knoll microstructure was mechanically compressed using SPM and the degree of compression increased under the increase in rolling force, as shown in Figures 5 and 6. Accordingly, the knoll region was not clearly distinguishable in Figure 5c,f. Because the adhesive strength is affected by the interfacial microstructure, it is understandable that interface flattening weakens the adhesive bonding and further flaking resistance. Therefore, when SPM elongation increased, the flaking resistance decreased. Meanwhile, the interface can also be flattened by excessive annealing. During annealing at high temperatures and/or long durations, the interface becomes flattened via lateral Γ phase growth, because the region under the Γ phase comprises flat interfaces which removes the etch-pit-shaped rough knoll [15]. Furthermore, interface flattening via thermal diffusion also reduces flaking resistance. The phenomenon and result are identical to the SPM case, though the cause is different: SPM flattening is a result of physical energy, whereas the interface flattening by excessive annealing is attributed to thermal energy. Consequently, the interface microstructure is strongly related to the adhesive bonding, and the interface flattening resulting from SPM reduces flaking resistance.

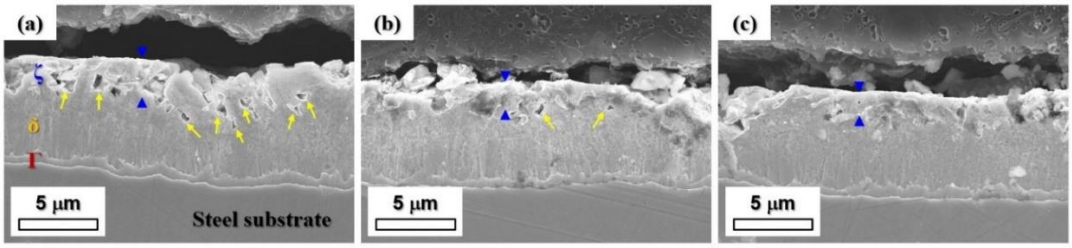

Figure 7. Cross-sectional FE-SEM micrographs of coating layer: (a) No-, (b) 1.8- and (c) 4.0-SPM.

Whilst flaking is related to the interface morphology, powdering is linked to the state of the coating interior, including the phase, microstructure, and defects. Figure 7a–c shows the cross-sectional microstructures of the coating layers for the No-, 1.8- and 4.0-SPM coatings, respectively. The coating consisted of the Γ, δ and ζ phases (from the bottom). Phases were arranged in an approximately layer-by-layer form, though the boundary between the δ and ζ phases was not clear. In Figure 7a, the ζ phase is intact and retains a columnar form, and pores are frequently observed there, as marked by yellow arrows. As shown in Figure 7b, some parts of the ζ phase were deformed and certain pores were accordingly filled after SPM elongation. In 4.0-SPM, pores were barely observed, as shown in Figure 7c. The layer became dense and uniform under an increase in SPM elongation. Figure 8 shows the fraction change of the Fe-Zn IMC phases under SPM elongation. The fraction was gradually affected by the SPM elongation. It is noteworthy that the fraction of ζ phases was significantly and gradually reduced from 15.9% to 9.8%, whereas that of the δ phase steadily increased from 74.6% to 80.0% under the increase in SPM elongation. In the case of the Γ phase, the fraction did not change considerably and was maintained around 10.3 ± 0.6%. Considering the change in the cross-sectional microstructure (Figure 7), the decrease in the fraction of ζ phases under SPM elongation is reasonable. Among the Fe-Zn IMCs, the ζ phase exhibited the highest plastic deformability [23]. It easily deformed under the rolling force in the SPM, as shown in Figures 3 and 7.

Therefore, when SPM was performed, the ζ phase was densified by plastic deformation, realized via pore filling. As a result, the ζ layer was thinned by densification and the deformation uniformly covered the coating surface, as indicated by the pair of blue arrowheads in Figure 7a–c.

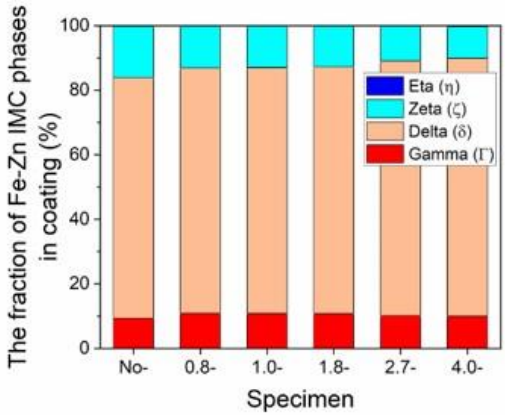

Figure 8. Fraction change of Fe-Zn intermetallic compound phases under SPM.

Figure 9a show the effective stress distribution in the SPM simulations under 4% elongation. This demonstrates that high stress occurred at the moment of rolling. Figure 9b indicates y-axis stress distribution. It is notable that some y-axis stress remained even after rolling although the stress value was small compared to the moment of rolling. To analyze the stress across the sheet (in the thickness direction) in detail, the stress range was modified in Figure 9c. It clearly shows that negative value of y-axis stress existed in the vicinity of the steel surface while positive value was in the center, as confirmed in Figure 9c and the inset. The stress distribution along the cross-section is shown in Figure 9d. It is worth noting that the stress is changed from positive to negative in the direction from the center to surface at the point of about 0.13 mm from the surface. It can be inferred that the whole GA coating layer becomes compressive state considering that the layer was only about 7 μm in thickness.

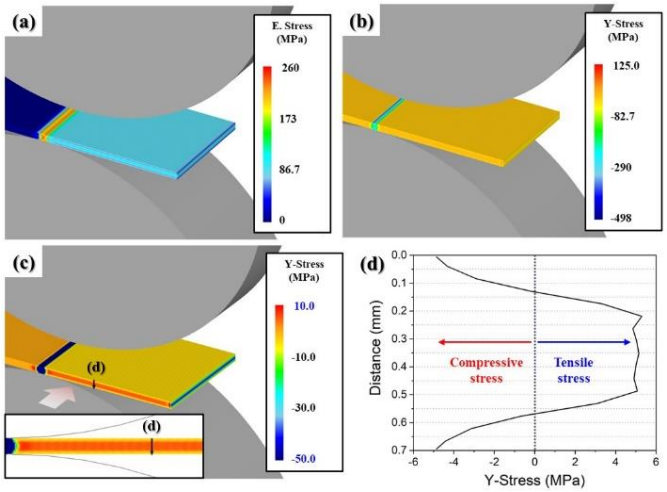

Figure 9. Simulation result of 4.0-SPM: (a) effective stress, (b) y-axis stress, (c) modified stress range of (b) (the inset indicates 2D stress distribution in the view of a pale red arrow) and (d) y-axis stress along the cross-section in the direction of a black arrow in (c).

Figure 10a–b shows the changes in the x- and y-axis stresses at the surface of the steel sheet (the point of monitoring gauge in Figure 1) with respect to time during rolling. In Figure 10a, the surface underwent a tensile stress of 106.0 MPa just before rolling but a significantly high compressive stress of −113.7 MPa during rolling in the x-axis direction. After rolling, the tensile stress increased again to 133.8 MPa. Then, it decreased and remained at 72.4 MPa. In the case of the y-axis stress, the surface underwent a severe compressive stress of more than −380 MPa before recovering to −5.0 MPa, as shown in Figure 10b. Consequently, strong compressive stress occurred on the surface of the steel sheet in both the x- and y-axis directions at the moment of rolling. However, significant tensile stress finally remained in the x-direction, whereas a little compressive stress remained in the y-direction. This is in good agreement with a previous report, in which mechanical surface treatments provided near-surface compressive residual stress [24–26].

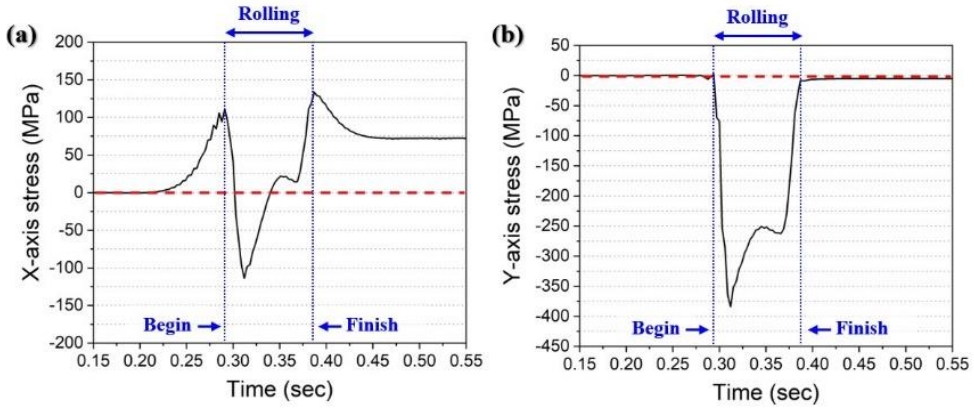

Figure 10. Change in the (a) x- and (b) y-axis stresses (as monitored by a surface gauge) with respect to time during rolling.

From the simulation results, three facts can be inferred: (1) High compressive stress at the moment of rolling produces flattening of the GA surface and interface between the coating and substrate. This results in deterioration of the flaking resistance. (2) The ζ layer undergoes significant plastic deformation and squashes in the x-direction, leading to a uniform coverage of the coating surface. It has been reported that cracks tend to nucleate in brittle phases (e.g., the Γ and δ phases [27,28]). However, the ζ phase suppresses crack penetration originated from the Γ and δ phases because of the relatively high critical stress intensity factor [29]. Therefore, the uniformly covered ζ layer could play a role in suppressing crack propagation, thereby improving the powdering resistance. (3) Mechanical surface treatment causes compressive stress to densify and harden the coating layer. After galvannealing, tensile residual stress remains in the GA coating layer, owing to the difference in thermal expansion between the coating layer and substrate [30]. However, it can be inferred that the residual stress can change from tensile to compressive after SPM. It is widely known that compressive stress suppresses crack propagation. Therefore, the SPM-induced compressive stress in the coating layer improves the resistance to crack propagation, leading to a reduction in powdering.

Figure 11 shows the relationship between the powdering (V-bending test) and flaking (hat-bead test) resistances. It can be clearly confirmed that under SPM elongation, the powdering and flaking resistances exhibit contrasting behaviors. When the SPM elongation increases, the resistance of

powdering improves, whereas that of flaking deteriorates. In other words, the resistances of powdering and flaking can be controlled within a certain range using the SPM.

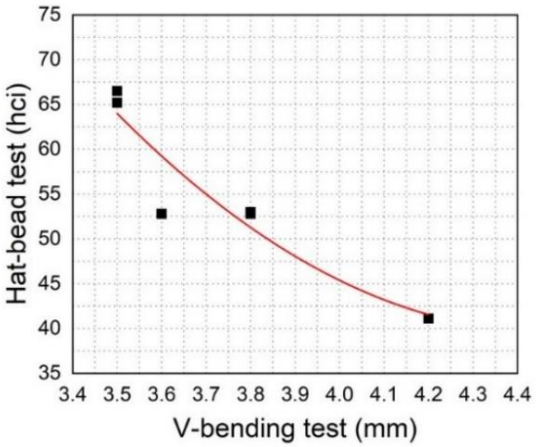

Figure 11. Relationship between V-bending and hat-bead tests under SPM.

4. Conclusions

In this study, the different behaviors of the powdering and flaking resistances of GA coatings were investigated using an SPM simulator and the underlying mechanisms were discussed via microstructural and simulation analyses. The main conclusions of this study are as follows:

(1) With respect to the SPM conditions, the contrasting behaviors between powdering and flaking were demonstrated. The resistance to powdering improved, whilst that to flaking deteriorated when the SPM elongation increased. This implies that the coating properties can be controlled within a certain range using the SPM process.

(2) A high compressive stress occurred on the surface of the steel sheet at the moment of SPM rolling. The stress caused flattening of the interface between the coating and substrate, in addition to the GA coating surface. Accordingly, rough knoll regions for mechanical interlocking (to reinforce the adhesive strength) lose their function. This interface flattening deteriorates the flaking resistance.

(3) During SPM elongation, the ζ layer in the coating is plastically deformed and the coating surface is uniformly covered by the ζ phase. Simultaneously, the coating layer is densified by the high compressive stress on the y-axis. This ζ phase covering and coating densification under compressive stress suppresses crack propagation, which improves powdering resistance.

(4) This conflicting behavior strongly supports the idea that the two failure types, powdering and flaking, are generated by different mechanisms. This implies that the two failure modes should be clearly distinguished and addressed from different perspectives, to improve their respective resistances.

We hope that this work will help address the current problems in GA coating research and industries, leading to more effective and efficient manufacturing procedures.

Use of AI tools declaration

The authors declare they have not used Artificial Intelligence (AI) tools in the creation of this article.

Acknowledgements

This study was supported by the Fundamental Research Program of the Korea Institute of Materials Science (PNK8920) and the Research and Development Center of Hyundai-Steel Company in the Republic of Korea.

Conflict of interest

The authors declare that there is no conflict of interest.

References

1. Shibli SMA, Meena BN, Remya R (2015) A review on recent approaches in the field of hot dip zinc galvanizing process. *Surf Coat Tech* 262: 210–215. https://doi.org/10.1016/J.SURFCOAT.2014.12.054
2. Marder AR (2000) The metallurgy of zinc-coated steel. *Prog Mater Sci* 45: 191–271. https://doi.org/10.1016/S0079-6425(98)00006-1
3. Inui H, Okamoto NL, Yamaguchi S (2018) Crystal structures and mechanical properties of Fe-Zn intermetallic compounds formed in the coating layer of galvannealed steels. *ISIJ Int* 58: 1550–1561. https://doi.org/10.2355/isijinternational.ISIJINT-2018-066
4. Yang D, Wang K, Zhou H, et al. (2023) Microstructure and properties of galvannealed coatings at different galvannealed time. *Mater Lett* 345: 134489. https://doi.org/10.1016/j.matlet.2023.134489
5. Okamoto NL, Inomoto M, Adachi H, et al. (2014) Micropillar compression deformation of single crystals of the intermetallic compound ζ-$FeZn_{13}$. *Acta Mater* 65: 229–239. https://doi.org/10.1016/j.actamat.2013.10.065
6. Garza LG, Van Tyne CJ (2007) Friction and formability of galvannealed interstitial free sheet steel. *J Mater Process Tech* 187: 164–168. https://doi.org/10.1016/j.jmatprotec.2006.11.062
7. Kancharla H, Mandal GK, Kumar RR, et al. (2022) Effect of annealing time on coating microstructure, frictional and electrochemical behavior of galvannealed interstitial-free steel. *J Mater Eng Perform* 32: 5932–5945. https://doi.org/10.1007/s11665-022-07527-4
8. Arimura M, Urai M, Iwaya J, et al. (1995) Effects of press-forming factors and flash plating on coating exfoliation of galvannealed steel sheets. Galvatech'95, The Use and Manufacture of Zinc and Zinc Alloy Coated Sheet Steel Products Into the 21 st Century, 733–738.
9. Claus G, Dilewijns J, De Cooman B, et al. (1995) Determination of the process window for optimal galvannealing of Ti-IF steel. Proceedings' Galvatech 95'ISS, Chicago, 107–113.
10. Hong MH (2005) Correlation between the microstructure of galvannealed coatings and the defoliation during press forming. *ISIJ Int* 45: 896–902. https://doi.org/10.2355/isijinternational.45.896
11. Lee KK, Lee IH, Lee CR, et al. (2007) In-situ observation in a scanning electron microscope on the exfoliation behavior of galvannealed Zn-Fe coating layers. *Surf Coat Tech* 201: 6261–6266. https://doi.org/10.1016/j.surfcoat.2006.11.021
12. Martin P, Handford MA, Packwood R, et al. (1992) Mechanical and structural study of Zn-Fe coatings on steel sheet. Galvatech'92, Amsterdam, 112–116.

13. Cheng C, Krishnardula V, Hahn H (2015) The effect of Al content in the coating on the flaking resistance of GA IF steels. International Conference on Zinc and Zinc Alloy Coated Steel Sheet, 96–103.
14. Han K, Lee I, Ohnuma I, et al. (2018) Micro-Vickers hardness of intermetallic compounds in the Zn-rich portion of Zn-Fe binary system. *ISIJ Int* 58: 1578–1583. https://doi.org/10.2355/isijinternational.ISIJINT-2018-111
15. Park H, Jeong YJ, Lee K, et al. (2020) Effect of galvannealing temperature on coating microstructure evolution correlated to flaking degradation on galvannealed interstitial-free steel. *Surf Coat Tech* 404: 126446. https://doi.org/10.1016/j.surfcoat.2020.126446
16. Park H, Jeong YJ, Lee K, et al. (2021) Correlation of interface microstructural features with the adhesive bonding strength of galvannealed interstitial-free steel. *Met Mater Int* 27: 3250–3259. https://doi.org/10.1007/s12540-020-00691-z
17. Hamers AJ, Koesveld WV, Schoen JP (1998) Stone chipping resistance, press behaviour and coating roughness of galvannealed IF steels. Galvatech'98, Chiba, 597–602.
18. Park H, Jeong YJ, Lee K, et al. (2020) Interface exfoliation mechanism of galvannealed steel sheet in bead-slide during press-forming. *Mater Today Commun* 25: 101669. https://doi.org/10.1016/j.mtcomm.2020.101669
19. Santos LA, Lopes LU, Wendhausen PAP (2014) Synthesis and characterization of the Fe-Zn intermetallic phases using the Rietveld Method. *Rem-Rev Esc Minas* 67: 181–184. http://dx.doi.org/10.1590/S0370-44672014000200008
20. Fluhrer J (2015) *DEFORM^{TM} 2D Version 8.1 User's Manual*, Columbus, Ohio: Scientific Forming Technologies Corporation.
21. Quang P, Krishnaiah A, Hong SI, et al. (2009) Coupled analysis of heat transfer and deformation in equal channel angular pressing of Al and steel. *Mater Trans* 50: 40–43. https://doi.org/10.2320/matertrans.MD200823
22. Wai Myint P, Hagihara S, Tanaka T, et al. (2017) Determination of the values of critical ductile fracture criteria to predict fracture initiation in punching processes. *J Manuf Mater Process* 1: 12. https://doi.org/10.3390/jmmp1020012
23. Okamoto NL, Kashioka D, Inomoto M, et al. (2013) Compression deformability of Γ and ζ Fe-Zn intermetallics to mitigate detachment of brittle intermetallic coating of galvannealed steels. *Scripta Mater* 69: 307–310. https://doi.org/10.1016/j.scriptamat.2013.05.003
24. Nikitin I, Besel M (2008) Residual stress relaxation of deep-rolled austenitic steel. *Scripta Mater* 58: 239–242. https://doi.org/10.1016/j.scriptamat.2007.09.045
25. Bhujangrao T, Veiga F, Penalva M, et al. (2022) Three-dimensional finite element modelling of sheet metal forming for the manufacture of pipe components: symmetry considerations. *Symmetry* 14: 228. https://doi.org/10.3390/sym14020228
26. Wang W, Hua D, Zhou Q, et al. (2023) Effect of a water film on the material removal behavior of Invar during chemical mechanical polishing. *Appl Surf Sci* 616: 156490. https://doi.org/10.1016/j.apsusc.2023.156490
27. Alpas AT, Inagaki J (2000) Effect of microstructure on fracture mechanisms in galvannealed coatings. *ISIJ Int* 40: 172–181. https://doi.org/10.2355/isijinternational.40.172
28. Nunomura Y, Takasugi T (2003) Plastic deformation and fracture behavior of galvannealed coating. *ISIJ Int* 43: 454–460. https://doi.org/10.2355/isijinternational.43.454

29. Ploypech S, Boonyongmaneerat Y, Jearanaisilawong P (2012) Crack initiation and propagation of galvanized coatings hot-dipped at 450 ℃ under bending loads. *Surf Coat Tech* 206: 3758–3763. http://dx.doi.org/10.1016/j.surfcoat.2012.03.029
30. Ochiai S, Okuda H, Iwamoto S, et al. (2005) Multiple-cracking phenomenon of the galvannealed coating layer on steels under thermal and tensile stresses. *Metall Mater Trans A* 36: 1807–1816. https://doi.org/10.1007/s11661-005-0044-0

AIMS Press